Growth kinetics of disk-shaped copper islands in electrochemical deposition

Lian Guo,[1] Shouliang Zhang,[2] and Peter Searson[1]
[1]*Department of Materials Science and Engineering, Johns Hopkins University, Baltimore, Maryland 21218, USA*
[2]*Department of Earth and Planetary Sciences, Johns Hopkins University, Baltimore, Maryland 21218, USA*
(Received 23 December 2008; published 1 May 2009)

The ability to independently dictate the shape and crystal orientation of islands in electrocrystallization remains a significant challenge. The main reason for this is that the complex interplay between the substrate, nucleation, and surface chemistry is not fully understood. Here we report on the kinetics of island growth for copper on ruthenium oxide. The small nucleation overpotential leads to enhanced lateral growth and the formation of hexagonal disk-shaped islands. The amorphous substrate allows the nuclei to achieve the thermodynamically favorable orientation, i.e., a $\langle 111 \rangle$ surface normal. Island growth follows power law kinetics in both lateral and vertical directions. At shorter times, the two growth exponents are equal to $\frac{1}{2}$ whereas at longer times lateral growth slows down while vertical growth speeds up. We propose a growth mechanism, wherein the lateral growth of disk-shaped islands is initiated by attachment of Cu adatoms on the ruthenium oxide surface onto the island periphery while vertical growth is initiated by two-dimensional nucleation on the top terrace and followed by lateral step propagation. These results indicate three criteria for enhanced lateral growth in electrodeposition: (i) a substrate that leads to a small nucleation overpotential, (ii) fast adatom surface diffusion on substrate to promote lateral growth, and (iii) preferential anion adsorption to stabilize the basal plane.

DOI: 10.1103/PhysRevE.79.051601 PACS number(s): 81.10.Dn, 68.55.A−, 81.15.Pq, 68.08.−p

I. INTRODUCTION

The study of nucleation and growth in electrocrystallization has a long history [1–5]. In the large overpotential regime, far from equilibrium, deposition usually occurs by Volmer-Weber island growth [6–14]. Under these conditions, control of island shape is not possible and deposition usually results in the formation of nonfaceted (hemispherical) islands. In the near-equilibrium regime, research has focused on epitaxial deposition [e.g., Ag on Ag(*hkl*) and Cu on Cu(*hkl*)] [1–4,15–17]. For these epitaxial systems with a layer-by-layer growth mode, the details of nucleation, propagation of step edges, and spiral growth at screw dislocations have been formulated [2,4,5]. Under these conditions control of island shape can be achieved, but island orientation is usually dictated by the substrate and cannot be controlled independently.

In crystal growth from aqueous solution, the evolution of surface morphology under near-equilibrium conditions has been widely studied, e.g., [18–31]. In contrast, the evolution of the surface morphology of islands in electrocrystallization (i.e., nonepitaxial systems that exhibit a Volmer-Weber island growth mode) is poorly understood. There are two main reasons for this. First, the nucleation overpotential, i.e., the energy barrier for nucleation on a foreign substrate, is usually 200 mV or more. Consequently, after nucleation, growth is too fast to achieve equilibrium structures. Second, the orientation of an island is usually determined by the crystal structure of the substrate.

Here we report on the kinetics of island growth during deposition of copper on amorphous ruthenium oxide. The island shape and orientation are determined by two key factors. First, the amorphous substrate dictates Cu island orientation by allowing the nuclei to achieve the thermodynamically favorable close-packed in-plane structure with a $\langle 111 \rangle$ surface normal. Second, by eliminating the influence of a crystalline substrate (grain size, crystal orientation, grain boundaries, dislocations, etc.), under near-equilibrium conditions, island growth can be controlled solely by surface energies of different facets. In previous work we have shown that deposition of copper on amorphous ruthenium oxide occurs with a very small nucleation overpotential, resulting in the formation of hexagonal disk-shaped islands [32]. The well-defined island geometry in this system provides an opportunity to study the growth kinetics in much greater detail than has previously been possible in electrodeposition. Here we show that island growth at short times follows a power law in both lateral and vertical directions, with exponents of $\frac{1}{2}$, while at longer times, lateral growth slows down while vertical growth speeds up. We propose a growth mechanism where the lateral growth of disk-shaped islands is initiated by attachment of Cu adatoms on the ruthenium oxide surface to the island periphery, and vertical growth is initiated by two-dimensional (2D) nucleation on the top terrace and followed by lateral step propagation. These results indicate three criteria for enhanced lateral growth in electrodeposition: (i) a substrate that leads to a small nucleation overpotential, (ii) fast adatom surface diffusion on the substrate to promote lateral growth, and (iii) preferential anion adsorption to stabilize the basal planes.

II. EXPERIMENTAL SECTION

Deposition of Cu was performed on ruthenium oxide on polycrystalline ruthenium in a standard electrochemical cell with a copper wire reference electrode and platinum mesh counter electrode. Nucleation and growth are relatively slow in the near-equilibrium regime and hence a Cu(II)/Cu reference electrode was used to avoid contamination during the relatively long experiments. All potentials are reported ver-

 ©2009 The American Physical Society

sus the copper wire reference electrode. Unless otherwise stated, experiments were performed in solution containing 0.1*M* $CuSO_4$ (99.999%, Alfa Aesar) and 0.2*M* H_2SO_4 (99.9999%, Alfa Aesar) in 18.2 MΩ de-ionized (DI) water (pH=1.03) at an applied potential of −64 mV (vs Cu^{2+}/Cu) and at 23 °C.

Experiments were also performed at potentials from −54 to −104 mV and at temperatures from 1 to 71 °C using a temperature controlled hot plate. The pH of the solution was adjusted by varying the concentrations of H_2SO_4:pH 0.44 (0.04*M* H_2SO_4), pH 1.03 (0.2*M* H_2SO_4), and pH 1.56 (1*M* H_2SO_4). The influence of Cu(II) concentration was studied in solutions with 0.01*M* $CuSO_4$, 0.1*M* $CuSO_4$, and 1.0*M* $CuSO_4$; in all cases the solution contained 0.2*M* H_2SO_4. The influence of anion was studied in solutions containing 0.1*M* $CuSO_4$ and 0.2*M* H_2SO_4, 0.1*M* $Cu(ClO_4)_2$ (99.999% metals basis, Alfa Aesar) and 0.2*M* $HClO_4$ (99.9985% metals basis, Alfa Aesar), and 0.1*M* $CuSO_4$, 0.2*M* H_2SO_4, and 1 mM HCl (ACS, Baker).

The substrate, which was prepared by physical vapor deposition of ruthenium on single crystal Si, is smooth with rms roughness of 1.8 Å over 2×2 μm^2 area [32]. The ruthenium has no in-plane ordering but has strong (002) texture with an average grain size of 14 nm and a native oxide about 2 nm in thickness [32].

Copper islands were examined by atomic force microscopy (AFM) (Molecular Imaging Pico-Plus), scanning electron microcopy (SEM) (JEOL 6700F) equipped with energy dispersive x-ray analysis (EDAX) Genesis 4000 microanalysis system, x-ray diffraction (Philips X'Pert four-circle system), as well as transmission electron microscopy (TEM) (Philips EM 420 and CM 300). Energy-filtered TEM images were acquired near the oxygen *K* edge using a post-column Gatan Imaging Filter in the Philips CM 300 TEM. In a typical experiment, after deposition the sample was rinsed in distilled water and at least five AFM images (50×50 μm^2) obtained at random locations on the sample using a 70 μm scanner.

Individual copper islands were characterized by TEM after removing from the substrate. After deposition from solution containing 0.1*M* $CuSO_4$ and 0.2*M* H_2SO_4 at −64 mV (vs Cu^{2+}/Cu) for 50 s, the sample was sonicated in distilled water for 30 min. After centrifugation for 5 min at 2000 rpm, the islands were resuspended in DI water, and then a drop of the suspension was placed on a lacey carbon TEM grid. Cross sections for transmission electron microscope analysis TEM were prepared by mechanical polishing and ion beam milling.

III. RESULTS AND DISCUSSIONS

A. Cu deposition

Figure 1(a) shows a current density versus time curve for copper deposition at −64 mV. In contrast to current-time curves for diffusion limited growth that are characterized by an initial increase in current due to isolated island growth followed by a decrease due to planar diffusion to the growing islands, the current-time curve shown here reveals more temporal information on island nucleation and growth. After an induction time, t_0, of 11 s copper starts to nucleate and the current increases sharply. At 20 s the slope of the current-time curve decreases, implying that nucleation has finished. This is confirmed by AFM image analysis (see below) showing that the island density is approximately constant after 20 s. The islands then grow, both laterally and vertically, until the suppression of lateral growth associated with island-island interactions leads to a decrease in the deposition current after about 700 s. Finally, the onset of island coalescence occurs at about 1000 s, after which the current density is approximately constant and determined by the vertical growth rate. AFM images of the disk-shaped islands after 20, 100, 500, and 1000 s, respectively, are presented in Fig. 1(b), illustrating that individual islands exhibit a hexagonal shape with lateral dimension much larger than the vertical dimension. The sequence of images clearly shows the progression from isolated island growth to island coalescence and the formation of a continuous film.

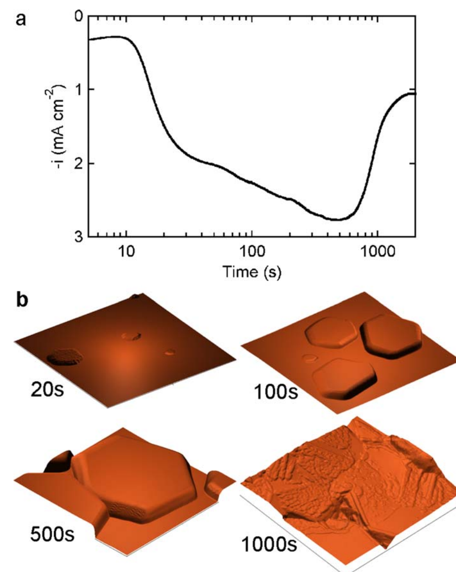

FIG. 1. (Color online) (a) Current density versus time for copper deposited from solution containing 0.1*M* $CuSO_4$ and 0.2*M* H_2SO_4 at −64 mV (vs Cu^{2+}/Cu) for 2000 s. (b) AFM images (8×8 μm^2) of disk-shaped islands at 20, 100, 500, and 1000 s depositions.

AFM images after 100 and 500 s (Fig. 2) show a distribution of island sizes due to the range of nucleation times (approximately 11–20 s). The images also show the existence of a small number of polygonal islands. Energy dispersive x-ray spectroscopy (EDS) indicates no compositional difference between the polygonal islands and the disk-shaped islands in the detection limit of the instrument (approximately 1 at. %). Figure 2(c) shows a histogram of the island near neighbor distances, which can be well fit by the Poisson distribution, indicating complete spatial randomness.

In order to confirm that the AFM images are representative of the whole surface, we compare the charge density obtained from integration of the current transient to the charge per unit area contained in the islands in the AFM images. The charge density obtained from integration of the deposition transient (solid line in Fig. 3) is proportional to

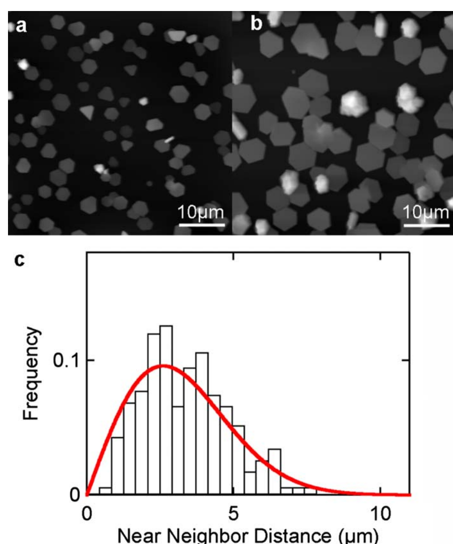

FIG. 2. (Color online) AFM images ($50 \times 50\ \mu m^2$) of copper from solution containing $0.1M$ $CuSO_4$ and $0.2M$ H_2SO_4 at -64 mV (vs Cu^{2+}/Cu) for (a) 100 s and (b) 500 s. (c) Near-neighbor-distance distribution obtained from analysis of 98 islands after 20 s. The solid line shows the Poisson distribution, confirming complete spatial randomness.

the average volume of copper deposited over the whole surface area. The volume of copper in each AFM image ($50 \times 50\ \mu m^2$) is obtained from the sum of the volume of each island and converted to a charge density using Faraday's law. The charge density is then averaged over at least five images randomly selected over the surface. The excellent agreement between the global average charge density and the charge density obtained from analysis of the AFM images, shown in Fig. 3, indicates that the island distribution is uniform and that the AFM images are representative of the whole surface.

The out-of-plane orientation of the copper islands was characterized by x-ray diffraction. As shown in Fig. 4, a Cu(111) peak is observed at the onset of deposition and becomes much stronger at longer times resulting from the growth of the hexagonal disk-shaped islands. At 200 s, a

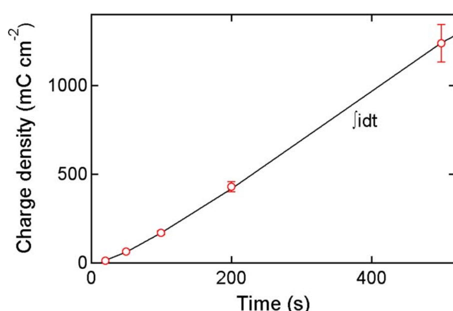

FIG. 3. (Color online) (Solid line) Deposition charge density obtained from integration of the current-time transient for copper deposited from solution containing $0.1M$ $CuSO_4$ and $0.2M$ H_2SO_4 at -64 mV (vs Cu^{2+}/Cu) at different times. (o) Charge density obtained from analysis of AFM images at different deposition times. The charge density was obtained from the volume of all islands in at least five $50 \times 50\ \mu m^2$ AFM images using Faraday's law.

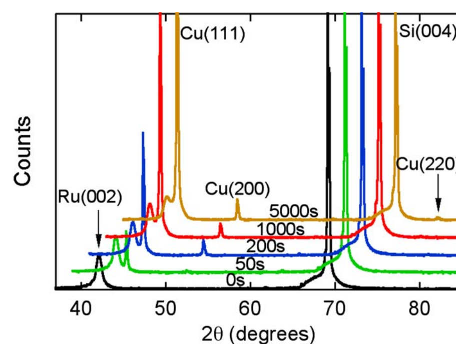

FIG. 4. (Color online) X-ray diffraction patterns for copper deposited from solution containing $0.1M$ $CuSO_4$ and $0.2M$ H_2SO_4 at -64 mV (vs Cu^{2+}/Cu) for 0, 50, 200, 1000, and 5000 s.

Cu(200) peak emerges as the total volume of the polygonal islands becomes sufficiently large to be detected, as illustrated in Fig. 2(b). The intensity of the Cu(200) peak remains approximately constant at longer times. After 1000 s, when the islands begin to coalesce, a very weak Cu(220) signal is identified. X-ray pole figure measurements confirmed that the disk-shaped islands have a random in-plane orientation on the substrate. The random in-plane orientation can be inferred from comparison of the edges of the hexagonal islands in Fig. 2.

Figure 5 shows a bright field TEM image of a hexagonal disk-shaped island with lateral dimension of about 2 μm, after removal from the substrate. The selected area diffraction pattern shows that the island is single crystal and confirms the $\langle 111 \rangle$ surface orientation. The interatomic spacing of 2.56 Å is in excellent agreement with the value for bulk copper [33]. The cross-section TEM image in Fig. 6 shows that the oxide layer on the ruthenium substrate between the disk-shaped copper islands and the ruthenium substrate is about 2 nm in thickness. There is no contrast change in the ruthenium oxide layer on tilting the specimen, implying that the oxide is amorphous.

An important consequence of the amorphous substrate is that island nucleation becomes decoupled from microstructural features that are intrinsic to crystalline substrates (e.g.,

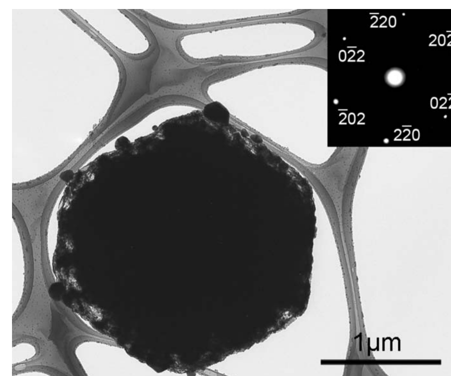

FIG. 5. TEM bright field image of a copper disk-shaped island deposited from solution containing $0.1M$ $CuSO_4$ and $0.2M$ H_2SO_4 at -64 mV (vs Cu^{2+}/Cu) for 50 s. The inset shows the corresponding selective area diffraction image with zone axis $\langle 111 \rangle$.

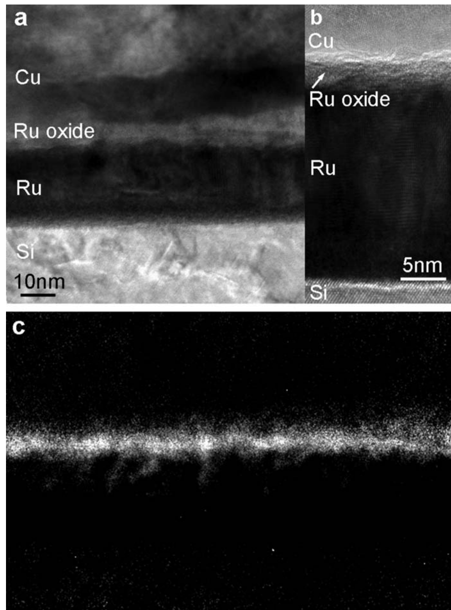

FIG. 6. (a) Zero-loss energy-filtered TEM (EFTEM) image of the cross section of Cu disk-shaped island electrodeposited on ruthenium substrate from solution containing $0.1M$ $CuSO_4$ and $0.2M$ H_2SO_4 at -64 mV (vs Cu^{2+}/Cu) for 200 s. (b) Higher magnification cross-section TEM image of the Cu island shown in (a). (c) The jump-ratio EFTEM image on the oxygen K edge for the image shown in (a).

grain size, crystal orientation, grain boundaries, dislocations, etc). Thus nuclei exhibit the thermodynamically favorable close-packed in-plane structure with a $\langle 111 \rangle$ surface normal. In addition, island growth under near-equilibrium conditions is controlled by the surface energies of different facets. Preferential adsorption of sulfate anions on the Cu(111) surface [34,35] stabilizes the basal plane and hence leads to the formation of disk-shaped islands.

Figure 7 shows the island density obtained from AFM images versus time up to 500 s, prior to the onset of coalescence, and hence allowing all individual islands to be easily distinguished. The overall island density N_0 increases and reaches a maximum of 3.6×10^6 cm^{-2} after 100 s. The majority of disk-shaped islands form before 20 s, and their number density increases slowly up to 100 s and then remains constant at 2.9×10^6 cm^{-2}. The polygonal islands appear after 20 s and their number density increases slowly over time but is still much less than the density of the disk-shaped islands. Figure 7 confirms the conclusion from the current-time curves that nucleation is almost complete after 20 s.

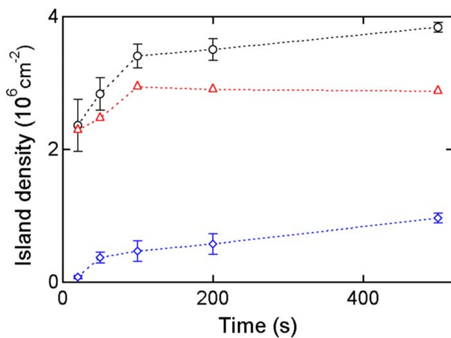

FIG. 7. (Color online) Density of copper islands deposited from solution containing $0.1M$ $CuSO_4$ and $0.2M$ H_2SO_4 at -64 mV (vs Cu^{2+}/Cu) versus deposition times for (△) disk-shaped islands, (◇) non-disk-shaped islands, and (○) all islands.

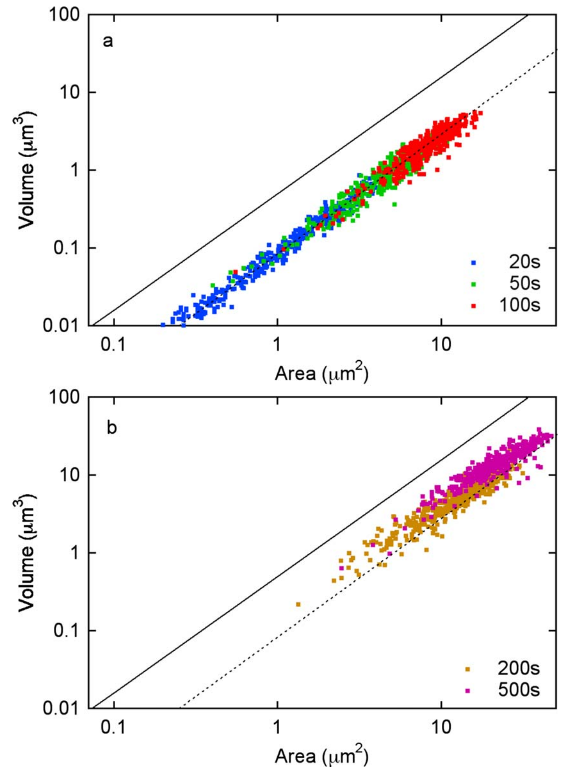

FIG. 8. (Color online) Volume versus area for disk-shaped islands deposited from solution containing $0.1M$ $CuSO_4$ and $0.2M$ H_2SO_4 at -64 mV (vs Cu^{2+}/Cu) after (a) 20, 50, and 100 s and (b) 200 and 500 s. The solid line corresponds to isotropic island growth and the dashed line represents the power law fitting of all data points up to 100 s. The number of islands at each deposition time were 379 (20 s), 402 (50 s), 363 (100 s), 403 (200 s), and 390 (500 s).

From these results we can conclude that the hexagonal disk-shaped islands have low aspect ratio with a $\langle 111 \rangle$ surface orientation, a random in-plane orientation, and are randomly distributed on the substrate. Nucleation occurs between 10–20 s and the onset of island coalescence occurs at about 500 s.

B. Growth kinetics

The evolution of island size and shape was determined from analysis of the volume and projected area of each island. Figure 8 shows a plot of volume versus projected area for the disk-shaped islands at different times. For each deposition time, all islands exhibit a broad distribution in volume and area due to their different nucleation times. From the island spatial randomness [Fig. 2(c)] it is reasonable to assume that each island grows independently and hence all islands obey the same growth law from which we can extract

kinetic information. The solid line in both figures represents the isotropic growth curve,

$$V = \frac{1}{2}A^{3/2}, \quad (1)$$

where V is the volume of the island, A is the projected area, and the exponent 3/2 defines the slope in the double-logarithmic plot. In Fig. 8(a), the volume and area of each island increases with increasing time from 20 to 100 s. However, all data points at different times can be well fitted by the same power law relation, represented by the dashed line in the figure, which is parallel to the isotropic growth curve and has the same exponent of 3/2. This observation leads to three conclusions. First, growth of the disk-shaped islands follows a power law in each dimension,

$$L \propto t^{a}, \quad (2a)$$

$$h \propto t^{b}, \quad (2b)$$

where L and h are the lateral and vertical dimensions, respectively, while a and b are the corresponding growth exponents. Experimentally, the island width and height are determined from the volume and the projected area measured by AFM,

$$L = A^{1/2}, \quad (3a)$$

$$h = V/A. \quad (3b)$$

Second, the lateral and vertical growth exponents are equal, i.e., $a=b$. Third, up to $t=100$ s the growth of the disk-shaped islands follows the same kinetic law. From the shift between the experimental data and the isotropic growth curve we can determine the ratio between the lateral growth rate and the vertical growth rate, which is about 6, i.e., the copper disks grow six times faster laterally than vertically. Note that the ratio between the lateral and vertical growth rates corresponds to the average width divided by the average height. Figure 8(b) shows that the growth of the disk-shaped islands starts to deviate from the power law after 100 s, indicating different growth kinetics. This change is due to the onset of interactions between islands, as illustrated in the AFM image for $t=500$ s in Fig. 1, resulting in the suppression of lateral growth. In this regime, lateral growth slows down while vertical growth speeds up.

To obtain the values of the growth exponents a and b we use two approaches. First, we analyze the time dependence of the total projected areas of all islands over the substrate by applying the Avrami theorem. Second, we analyze the average lateral dimension (island diameter) and the average vertical dimension (island height) of the disk-shaped islands at different times.

The transformed area resulting from randomly distributed islands for both long and short times can be described by Kolmogorov-Johnson-Mehl-Avrami (KJMA) equation [36–38],

$$f = 1 - \exp[-S(t)] = 1 - \exp(-kt^{n}), \quad (4)$$

where f is the fractional surface coverage by the islands, $S(t)$ is the extended surface coverage, k is the rate constant, and n is a numerical exponent whose value can vary from 1 to 4. In Fig. 9 we plot $-\ln(1-f)$ versus $t-t_0$ and from the slope we obtain an exponent $n=1$. Since $L \propto A^{1/2}$, we obtain a lateral growth exponent $a=1/2$ and hence $a=b=1/2$. In two dimensions, the exponent $n=1$ indicates instantaneous nucleation and surface diffusion limited growth [39]. Instantaneous nucleation is self-evident since the nucleation time (about 10 s) is much less than the growth period (about 1000 s). From the slope of the plot of $-\ln(1-f)$ versus $t-t_0$, we obtain a rate constant $k=1/350\ \text{s}^{-1}$. At short times $t \leq 100$ s, the exponential term in Eq. (4) is quite small indicating that island-island interactions can be neglected. This is consistent with the kinetic transition occurring between 100 and 200 s.

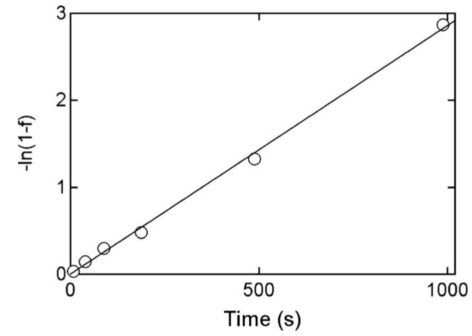

FIG. 9. Plot of $-\ln(1-f)$ versus $t-t_0$ according to the KJMA equation. The data were obtained from analysis of AFM images of copper deposition from solution containing 0.1M $CuSO_4$ and 0.2M H_2SO_4 at −64 mV (vs Cu^{2+}/Cu). The fractional coverage f was obtained from analysis of all islands in eight randomly selected AFM images ($50 \times 50\ \mu m^2$). The linear relation indicates that the electrocrystallization mechanism is instantaneous nucleation with diffusion-controlled growth.

Figure 10 shows the time dependence of the average island diameter, island height, and aspect ratio. The island lateral dimension shows two kinetic regimes consistent with isolated island growth up to 100 s and coupled island growth after 100 s (see Fig. 8). In the isolated island growth regime, we obtain a lateral growth exponent $a=0.47$. In the coupled growth regime lateral growth slows down due to island impingement and the exponent becomes smaller. As shown in Fig. 10(b), vertical growth also has two kinetic regimes, indicating the correlation between vertical and lateral growths. In the isolated island growth regime we obtain a vertical growth exponent $b=0.45$, almost identical to the lateral growth exponent a and consistent with the conclusion drawn from Fig. 8(a). In the coupled growth regime, vertical growth speeds up due to the suppression of lateral growth and the exponent becomes larger.

Figure 10(c) shows the aspect ratio of disk-shaped islands, which is the vertical dimension divided by the lateral dimension. Note that the aspect ratio of 1/12 (height/diameter) corresponds to a growth rate ratio of 6 (lateral growth rate divided by vertical growth rate). Up to 100 s, the aspect ratio remains constant since the two exponents a and b are equal, indicating that island growth is self-similar. After 100 s, the aspect ratio increases, and islands grow taller due to the suppression of lateral growth.

In summary, disk-shaped island growth follows a power law with growth exponents of 1/2 in both lateral and vertical

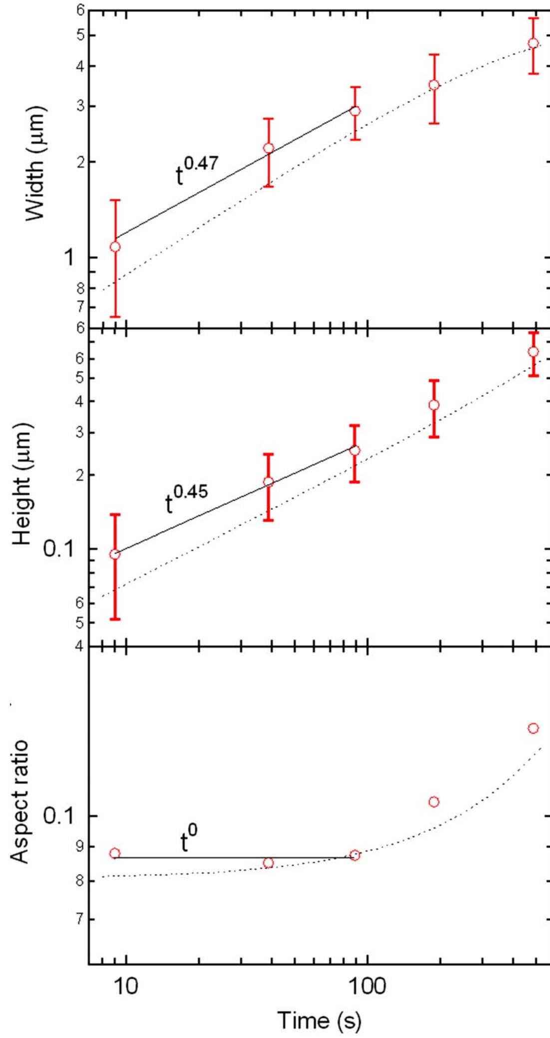

FIG. 10. (Color online) Time dependence of (a) average island diameter, (b) average island height, and (c) average aspect ratio (height/diameter) for hexagonal disk-shaped islands. The data were obtained from analysis of AFM images of copper deposition from solution containing 0.1M $CuSO_4$ and 0.2M H_2SO_4 at −64 mV (vs Cu^{2+}/Cu). The average lateral and vertical dimensions were obtained from analysis of all islands in at least five randomly selected AFM images (50×50 μm^2). The solid lines are the power law fits for experimental data up to 100 s. The dotted lines show results from Eqs. (9) and (10), taking $N_0=3.6\times 10^6$ cm^{-2}, $k=1/350$ s^{-1}, $m=10$, $v=0.8$ μm s^{-1}, and $d=2$ Å. N_0 was obtained from analysis of AFM images, k was determined from a fit to the Avrami plot (Fig. 9), the number of steps on the top terrace involved in lateral propagation m was estimated from AFM images (Fig. 12), the step propagation rate v was determined from Eq. (8) assuming that the vertical growth rate is limited by step propagation, and the step height d was determined from the lattice parameter. The time axis for the dotted line was offset by the induction time, $t_0=11$ s.

directions. The growth exponents obtained from the simple arithmetic mean of the island dimensions (Fig. 10), disregarding the size distribution and the influence of polygonal islands, are in good agreement with the exponents obtained from analysis of the extended area (Fig. 9).

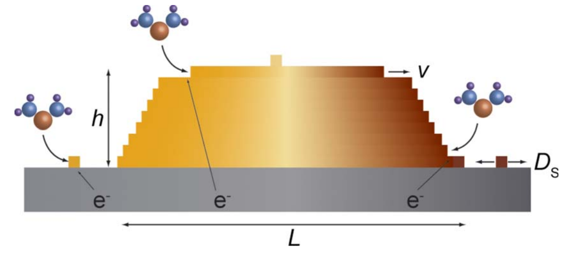

FIG. 11. (Color online) Schematic illustration of the mechanism of growth for the disk-shaped islands. Reduction in solvated copper ions at the surface results in copper adatoms on the substrate and on growing islands. Lateral propagation of steps on top of the island contributes to vertical growth. Lateral growth is initiated by diffusion limited adatom attachment at the perimeter of the island followed by reduction in copper ions on the step edges.

C. Growth mechanism

From our analysis of the island growth kinetics, we can comment on the growth mechanism of the disk-shaped islands (see Fig. 11). At the onset of deposition, reduction in Cu(II) ions on the substrate results in the formation of copper adatoms. This process is relatively slow due to the small driving force (overpotential). The formation of stable nuclei, after an induction time of about 11 s, results in a large increase in the deposition current since Cu(II) reduction is much faster on copper islands compared to the ruthenium oxide substrate. Lateral growth is initiated by the attachment of Cu adatoms on the substrate onto the island perimeter, then followed by fast Cu(II) reduction in the Cu step edges. By serving as a sink for Cu adatoms, the disk-shaped islands develop a depletion zone around the perimeter. When these depletion zones are isolated, each island grows independently according to $t^{0.5}$ [40]. However, when the depletion zones start to overlap, lateral island growth becomes coupled and hence slows down as indicated in Fig. 10.

The surface diffusion coefficient D_S for Cu adatoms on the ruthenium oxide substrate can be estimated from the average spacing and the crossover point. The island density of 3.6×10^6 cm^{-2} leads to an average island spacing of 5.3 μm and hence at the crossover point ($t=100$ s), we estimate $D_S\approx 2\times 10^{-10}$ cm^2 s^{-1}. Due to the complexity brought about by the substrate, applied potential, electrolyte, and temperature, it is not possible to make meaningful comparisons to other systems.

Vertical growth is associated with 2D nucleation and subsequent step flow on the Cu(111) terrace toward the terrace boundary. This process has two characteristic times: the nucleation interval τ and the time t_1 to grow a monolayer after nucleation [1]. If $\tau \gg t_1$, nucleation is so slow that it limits the vertical growth of the island. In this case the vertical growth rate is constant and given by d/τ, where d is the height of a single monolayer, resulting in a power law dependence $h\propto t^1$, which disagrees with our experimental observation. AFM images (Fig. 12) reveal multiple steps further suggesting that nucleation is not the rate limiting step. This kind of step structure has been observed at the solid/liquid interface for homoepitaxial and heteroepitaxial systems including Cu on Cu(111) [35,41], Ag on Ag(111) [41],

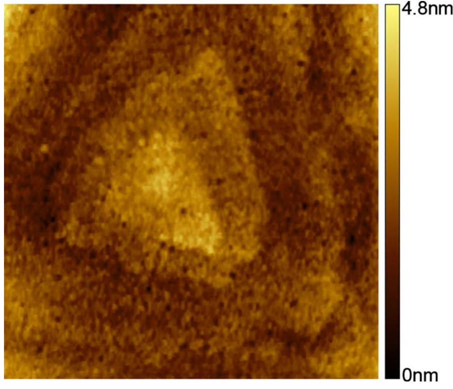

FIG. 12. (Color online) *Ex situ* AFM image ($2.8\times2.8\ \mu m^2$) of the top surface of a disk-shaped island after copper deposition from solution containing 0.1M $CuSO_4$ and 0.2M H_2SO_4 at −64 mV (vs Cu^{2+}/Cu) for 100 s. The image shows pyramid of growth consisting of 2D islands formed on top of each other; this structure was observed on all disk-shaped islands studied.

and Cu or Ni on Ag(111) [42,43]. Here we show islands with a step structure but formed on a noncrystalline substrate.

If $\tau<t_1$, then the vertical growth is rate limited by step propagation [1]. The time to complete one monolayer is $L/2v$, where L is the lateral dimension and v is the step propagation rate, which is generally considered as constant at a fixed overpotential [1,3]. Thus, the vertical growth rate is inversely proportional to the lateral dimension L, providing the coupling between vertical and lateral growths. At short times, from the power law for lateral growth $L\sim t^{0.5}$, we have $h\sim t^{0.5}$ which agrees with the experimental result. At longer times, lateral growth slows down due to the competition for Cu adatoms so that steps on the top terraces take less time to reach the boundary, resulting in faster vertical growth. This long time behavior qualitatively agrees with our experimental observations. Finally, we note that the triangular shape of the terraces seen in Fig. 12 might result from the different propagation rates of the two types of step on the Cu(111) terrace, while the overall hexagonal shape of the island is due to the nature of the noncrystalline substrate where the difference between two types of step disappears.

From the mechanism described above, we can derive an expression for the anisotropic growth ratio α, i.e., the lateral growth rate over the vertical growth rate, for isolated islands. First, for surface diffusion limited lateral growth of a single island we have [40]

$$L/2=\sqrt{2D_S\theta_c t},\tag{5}$$

where θ_c is the critical surface coverage of adatoms, whose value can be roughly estimated in the following way. At short times, $f\approx L^2N_0=8N_0D_S\theta_c t$ for instantaneous nucleation disregarding the island size dispersion. At the same time, at short times, $f\approx S(t)=kt$, where k is known from the Avrami analysis, and hence, $\theta_c\approx k/8N_0D_S=0.5$.

As described previously, for vertical growth limited by step propagation, the time to complete one monolayer is $L/2v$ and hence the rate law for vertical growth can be written as

$$\frac{dh}{dt}=\frac{mvd}{L/2}=\frac{mvd}{\sqrt{2D_S\theta_c t}},\tag{6}$$

where m is the number of steps on the top terrace involved in lateral propagation, d is the step height, and v is the step propagation rate. The time dependence of the island height is given by

$$h=mvd\sqrt{\frac{2t}{D_S\theta_c}}.\tag{7}$$

Combining Eqs. (5) and (7) we obtain an expression for the anisotropic growth ratio,

$$\alpha=\frac{L(t)/2}{h(t)}=\frac{D_S\theta_c}{mvd}.\tag{8}$$

Notice that the anisotropic growth ratio α is independent of time in the isolated growth stage, as indicated in Fig. 10(c). Choosing $\alpha=6$, $D_S=2\times10^{-10}\ \text{cm}^2\ \text{s}^{-1}$, $d=2$ Å, $m=10$ (see Fig. 12), and $\theta_c\approx0.5$, we obtain a step propagation rate $v=0.8\ \mu\text{m s}^{-1}$ at a potential of −64 mV.

If we assume that the islands are monodisperse, the fractional coverage is approximately $f=L^2N_0$. Combining with the KJMA equation, we obtain an expression for the average island width up to the onset of island coalescence,

$$L(t)=\frac{1}{\sqrt{N_0}}(1-e^{-kt})^{1/2}.\tag{9}$$

Substituting Eq. (6) into Eq. (9) and integrating, we obtain the corresponding expression for the island height

$$h(t)=2mvd\sqrt{N_0}\int_0^t(1-e^{-k\tau})^{-1/2}d\tau.\tag{10}$$

Substituting experimental values for N_0 and k, as well as the estimated value of mv from above, we plot island growth curves in Fig. 10. For both vertical growth and lateral growth, the model shows reasonable agreement with the experimental results and successfully reproduces the kinetic transition at about 100 s.

Moreover, the current density can be derived from Eqs. (9) and (10) using Faraday's law,

$$i(t)=nFN_0\frac{V'(t)}{V_m}=\frac{nFN_0}{V_m}[A'(t)h(t)+A(t)h'(t)],\tag{11}$$

where V_m is the molar volume (7.11 $\text{cm}^3\ \text{mol}^{-1}$ for Cu), F is Faraday's constant, n is the number of electrons ($n=2$ for Cu), and the two terms in brackets represent lateral growth and vertical growth, respectively. Figure 13 shows the total current and the contributions from lateral and vertical growths obtained from Eq. (11). The total current captures the crossover from isolated island growth to impingement of diffusion zones, however, the current maximum occurs at 320 s, somewhat earlier than the value of 520 s from experiments. Note that the lateral growth current reaches a maximum at 189 s, whereas the total current does not reach a maximum until 320 s, showing a considerable delay. This

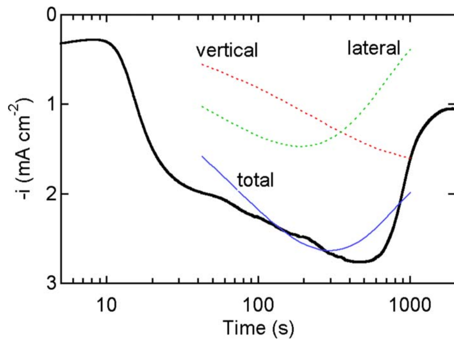

FIG. 13. (Color online) Deposition current versus time. Calculated contributions to the deposition current (see Fig. 1) from vertical and lateral growths, obtained from Eq. (11) where $V_m = 7.11\ \text{cm}^3\ \text{mol}^{-1}$ and $n=2$.

explains why the measured current starts to decrease as late as 500 s when a significant number of islands have coalesced [Fig. 2(b)].

D. Other electrodeposition conditions

Exploring the optimal conditions for growing disk-shaped islands, promoting lateral growth, and eliminating the polygonal islands, electrodeposition experiments were performed to determine the influence of overpotential, Cu concentration, sulfuric acid concentration, temperature, and anion.

1. Influence of potential

The formation of disk-shaped islands is observed in the potential range from −20 to −120 mV. Figure 14 shows SEM images of copper deposited from solution containing $0.1M$ $CuSO_4$ and $0.2M$ H_2SO_4 (pH 1.03) at 23 °C and at different overpotentials, illustrating that the islands become less faceted and lose the distinct (111) surface orientation at higher overpotentials. No deposition is discernible at lower overpotentials. The island density increases exponentially with increasing overpotential, with an inverse slope of $31\ \text{mV decade}^{-1}$ [32], much smaller value than typical values of 100–200 mV [11,44]. Deposition at –64 mV reveals the lowest density of polygonal islands and hence the largest fraction of disk-shaped islands. Furthermore, AFM characterization indicates that there is no significant difference in the aspect ratio of the disk-shaped islands at different deposition potentials.

The corresponding current-time curves, shown in Fig. 15(a), have similar features in this range of overpotentials: after a short induction time, the current density increases sharply when nucleation occurs, then becomes approximately constant indicating stable island growth, and finally decreases dramatically at the onset of coalescence. As the overpotential increases, the magnitude of deposition current increases and all events occur at shorter times. From the charge density at the current maximum, we can estimate the critical thickness for island coalescence d_{crit} [45]. As shown in Fig. 15(b), the critical film thickness is exponentially dependent on overpotential with a slope

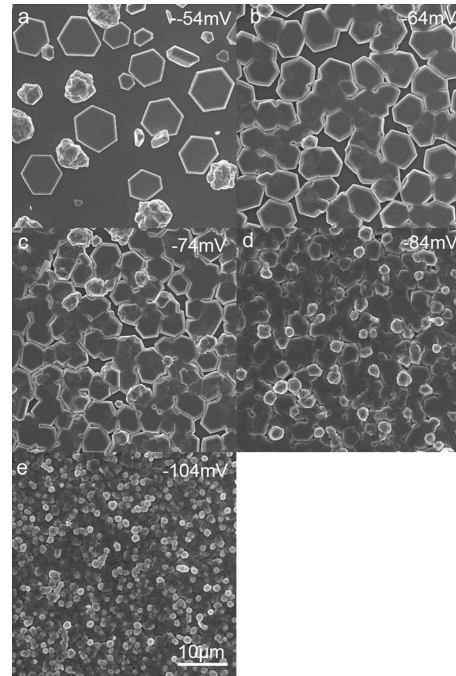

FIG. 14. Influence of deposition potential on island growth. Plan view SEM images for copper deposited from solution containing $0.1M$ $CuSO_4$ and $0.2M$ H_2SO_4 at (a) −54, (b) −64, (c) −74, (d) −84, and (e) −104 mV (vs Cu^{2+}/Cu). The deposition time was 1000 s except for −104 mV where the deposition time was 500 s.

$\partial d_{\text{crit}}/\partial\eta = -70\ \text{mV decade}^{-1}$. The island aspect ratio remains approximately constant in this potential range and hence we can take $d_{\text{crit}} \propto N_0^{-1/2}$ [45]. Taking the dependence of island density on potential from above ($\partial N_0/\partial\eta = 31\ \text{mV decade}^{-1}$), we predict that the slope in Fig. 15(b) to be $\partial d_{\text{crit}}/\partial\eta = -62\ \text{mV decade}^{-1}$, in good agreement with the observed value.

Figure 15(b) represents the minimum thickness at which island coalescence results in the formation of a continuous thin film. Although larger overpotentials allow the deposition of thinner films, overpotentials less than 120 mV are needed in order to deposit films comprised of disk-shaped islands with (111) texture.

An important feature of electrochemical deposition on foreign substrates is the existence of a nucleation overpotential η_c below which the nucleation does not occur. This barrier has been exploited to deposit metal nanoparticles with a narrow size distribution [46] and to deposit compact thin metal films [47]. Here we see that $\eta_c < 20$ mV, much smaller than typical values, for example, $\eta_c = 300$ mV for Pt on Ru(110) single crystal [48], $\eta_c > 600$ mV for Cu on TaN (depending on solution chemistry) [49], and $\eta_c > 120$ mV for Ag on TiN or the native oxide of Ru [50]. Our results suggest that the formation of disk-shaped islands is associated with the exceptionally small nucleation overpotential. For large nucleation overpotentials, the growth rate after nucleation is fast thereby limiting the ability of metal atoms to find their lowest energy lattice sites and resulting in hemispherical islands as well as isotropic growth.

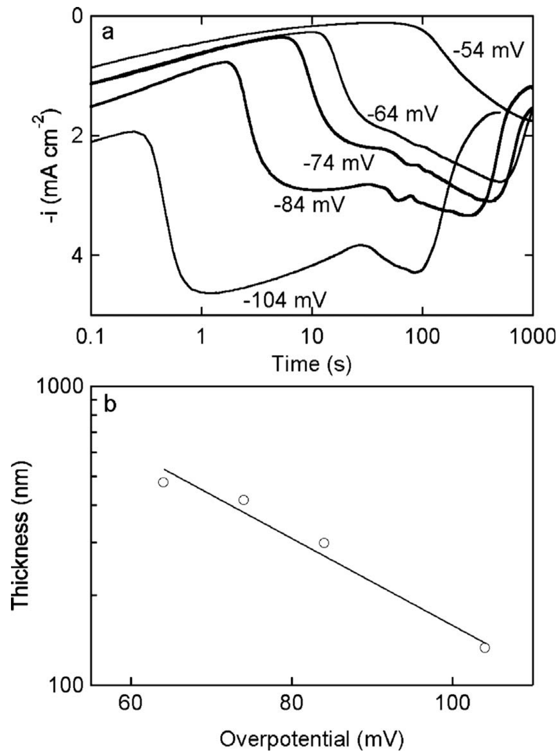

FIG. 15. (a) Current-time curves for copper deposition from solution containing $0.1M$ $CuSO_4$ and $0.2M$ H_2SO_4 at different overpotentials. (b) The potential dependence of nominal film thickness at coalescence. The film thickness was determined from the deposition charge density at the time when the current starts decreasing in the current-time curve.

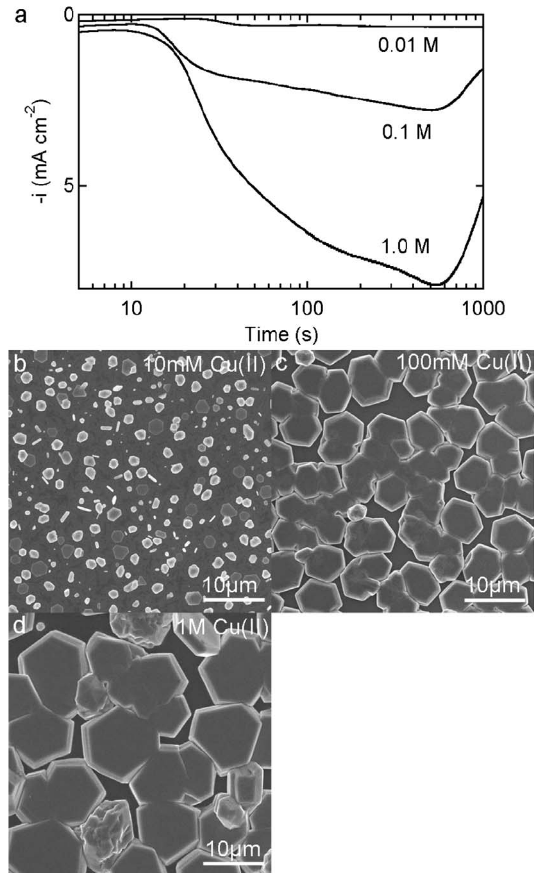

FIG. 16. Influence of Cu(II) concentration on island growth. (a) Current-time curves for copper deposition at −64 mV for solutions with Cu(II) concentrations of 10 mM, 100 mM, and $1M$. Plan view SEM images for copper deposited for 1000 s from solution containing (b) $0.01M$ $CuSO_4$, (c) $0.1M$ $CuSO_4$, and (d) $1.0M$ $CuSO_4$. In all cases the solution contained $0.2M$ H_2SO_4. Note that the deposition overpotential is 64 mV at all concentrations since we use a Cu(II)/Cu reference electrode; however, the equilibrium potential decreases by 30 mV per order of magnitude decrease in Cu(II) concentration.

2. Influence of Cu(II) concentration

The influence of Cu(II) concentration on island growth was studied from solution containing xM (x=0.01, 0.1, or 1) $CuSO_4$, 0.2 H_2SO_4 at −64 mV [vs Cu(II)/Cu] for 1000 s at 23 °C. Figure 16 shows that with increasing Cu(II) concentration, the current density increases, indicating fast island growth. Depositions at $0.1M$ and $1M$ Cu(II) both show current peaks at about 500 s, characteristic of island coalescence, as can be seen from the SEM images. For deposition in 10 mM Cu(II), there is no well-defined current peak. Since it is the suppression of enhanced lateral growth resulting from island coalescence that gives rise to the current peak, the lack of a well-defined peak indicates that anisotropic lateral growth is not dominant and implies that there is a significant fraction of polygonal islands. This is confirmed from the SEM image [Fig. 16(b)].

From Fig. 16(b) it can be seen that the island density increases with decreasing Cu(II) concentration. This effect may be due to differences in the adatom mobility since the rate of surface diffusion is believed to decrease with increasing negative potentials [51,52]. Although the deposition overpotential, and hence the thermodynamic driving force for copper deposition on copper, is maintained fixed at −64 mV, the equilibrium potential of Cu(II)/Cu reference electrode decreases by 30 mV per order of magnitude decrease in Cu(II) concentration. Thus, the absolute electrode potential becomes more negative with decreasing Cu(II) concentration.

Comparison of results examining the influence of deposition potential and Cu(II) concentration is that increasing the Cu(II) concentration is more effective than decreasing the overpotential in increasing the grain size. For example, film coalescence occurs at about 500 s for $1.0M$ Cu(II) at −64 mV, whereas coalescence in $0.1M$ Cu(II) at −54 mV occurs at times in excess of 1000 s [Fig. 15(a)].

3. Influence of pH

Figure 17 shows current-time transients and SEM images for deposition in $0.1M$ Cu(II) at −64 mV and at 23 °C with $0.04M$, $0.2M$, or $1.0M$ H_2SO_4. The current-time curves show that low acid concentration (increasing pH) favors island growth but impedes the nucleation, as can be seen from the increase in induction time. The absence of a well-defined current maximum in $1.0M$ H_2SO_4 (pH 0.44) suggests a significant fraction of non-disk-shaped islands and is confirmed

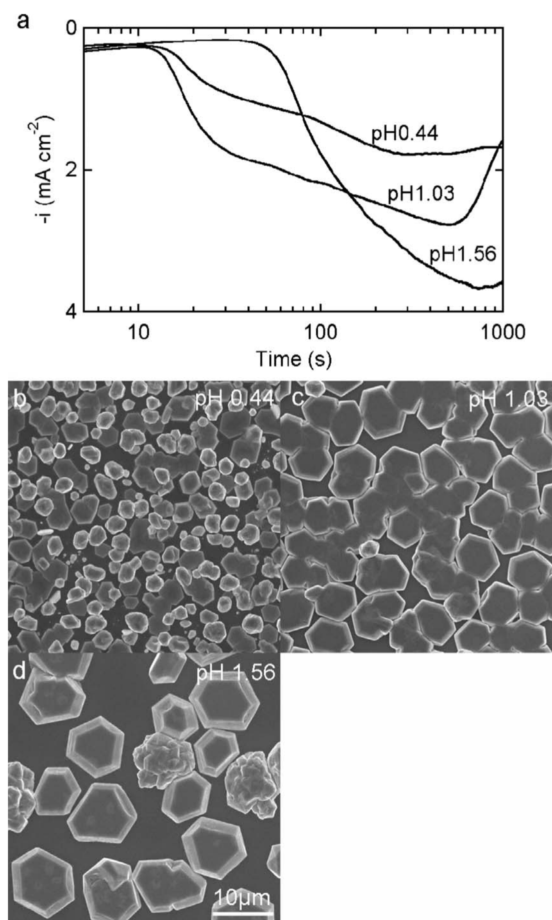

FIG. 17. Influence of pH on island growth. (a) Current-time curves for copper deposition at −64 mV from solution containing 0.1M $CuSO_4$ at pH 0.44 (0.04M H_2SO_4), pH 1.03 (0.2M H_2SO_4), and pH 1.56 (1M H_2SO_4). Plan view SEM images for copper deposited for 1000 s at (b) pH 0.44 (0.04M H_2SO_4), (c) pH 1.03 (0.2M H_2SO_4), and (d) pH 1.56 (1M H_2SO_4).

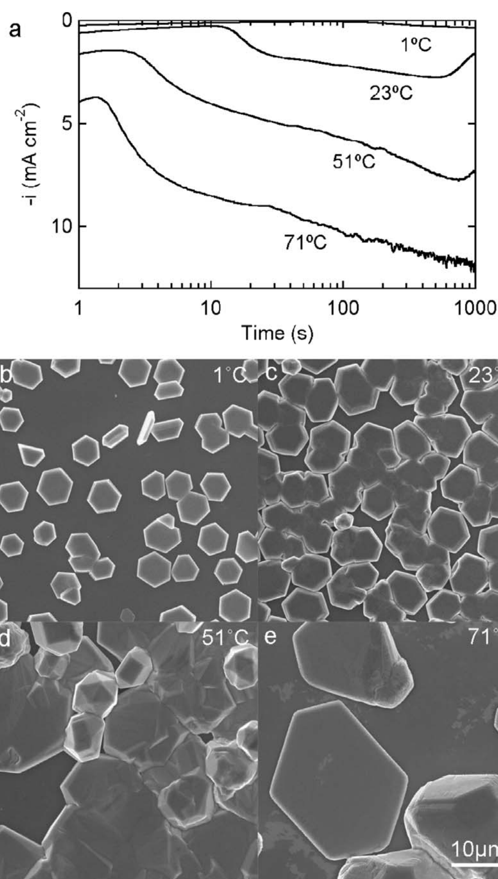

FIG. 18. Influence of temperature on island growth. (a) Current-time curves for copper deposition from solution containing 0.1M $CuSO_4$ and 0.2M H_2SO_4 at −64 mV at 1, 23, 51, and 71 °C. Plan view SEM images for copper deposited for 1000 s at (b) 1, (c) 23, (d) 51, and (e) 71 °C.

by the SEM image [Fig. 17(b)]. Besides, SEM images show that more acidic solution leads to larger island density.

4. Influence of temperature

Figure 18 shows current-time transients and SEM images for deposition from 0.1M $CuSO_4$ and 0.2M H_2SO_4 (pH 1.03) at −64 mV (vs Cu^{2+}/Cu) at temperatures from 1 to 71 °C. Increasing the temperature decreases the induction time for nucleation from about 200 s at 1 °C to less than 2 s at 71 °C. The absence of a well-defined current peak at 1 and 71 °C indicates slow island coalescence or that anisotropic lateral growth is not dominant. The SEM image at 1 °C shows the prevalence of disk-shaped islands, which are well separated from each other due to the slow growth rate at low temperature. At 71 °C, all islands are isolated due to the low island density despite of their fast growth rates, and the fraction of disk-shaped islands is relatively small. The current, and hence flux of copper atoms to the surface, increases with increasing temperature [Fig. 18(a)]. The increase in flux would be expected to result in an increase in the island density. On the other hand, elevated temperatures result in fast adatom surface diffusion rates, which is expected to decrease the island density. As a result, a maximum island density is seen at intermediate temperatures, 23 °C in our experiments, as shown in Fig. 18.

5. Influence of anion

Figure 19 shows SEM images for deposition of copper from 0.1M Cu(II) and 0.2M H_2SO_4 (pH 1.03) at −64 mV (vs Cu^{2+}/Cu) and at 23 °C with the anions SO_4^{2-}, ClO_4^-, and Cl^-. Sulfate anions preferentially adsorb on the Cu(111) surface [34,35], and chloride anions can adsorb on any Cu low index plane [53]. On the other hand, perchlorate anions do not specifically adsorb on most metals, including Cu [53]. In perchlorate solution under the same deposition conditions, nodular polycrystalline islands, rather than disk-shaped islands, are formed [Fig. 19(c)]. Similarly, chloride anions result in the formation of slightly branched islands [Fig. 19(b)]. Those two control experiments reveal that preferential adsorption of sulfate anions is critical in stabilizing the Cu(111) basal plane, defining the anisotropic growth direction and thus enhancing lateral growth.

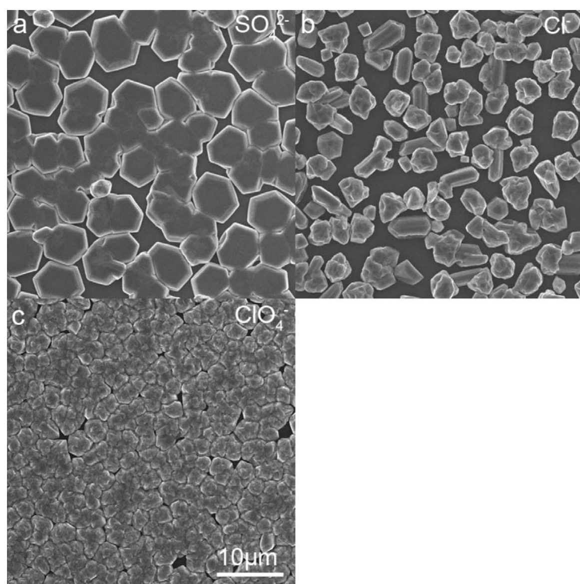

FIG. 19. Influence of anion on island growth. (a) Current-time curves for copper deposition at −64 mV from solution containing 0.1*M* $CuSO_4$ and 0.2*M* H_2SO_4, 0.1*M* $Cu(ClO_4)_2$ and 0.2*M* $HClO_4$, and 0.1*M* $CuSO_4$, 0.2*M* H_2SO_4, and 1 mM HCl. Plan view SEM images of copper deposited at −64 mV from solution containing (a) 0.1*M* $CuSO_4$ and 0.2*M* H_2SO_4, (b) 0.1*M* $Cu(ClO_4)_2$ and 0.2*M* $HClO_4$, and (c) 0.1*M* $CuSO_4$, 0.2*M* H_2SO_4, and 1 mM HCl. In all cases the deposition charge density was 2.3 C cm^{-2}.

IV. CONCLUSIONS

We have reported on the growth of Cu islands on ruthenium oxide, a system demonstrating enhanced lateral growth and resulting in the formation of low aspect ratio disk-shaped islands. The island shape is determined by two key factors: first, the amorphous substrate eliminates the influence of defects associated with crystalline substrates, allowing nuclei to achieve the thermodynamically favorable configuration with a $\langle 111 \rangle$ surface normal; second, preferential adsorption of sulfate anions on the Cu(111) surface stabilizes the basal plane.

Island growth follows power law kinetics in both lateral and vertical directions. At shorter times, the two growth exponents are equal to $\frac{1}{2}$, whereas at longer times lateral growth slows down while vertical growth speeds up. A growth mechanism, which explains experimental results semiquantitatively, has been proposed wherein the lateral growth of disk-shaped islands is initiated by attachment of Cu adatoms on the ruthenium oxide surface onto the island periphery while vertical growth is initiated by 2D nucleation on the top terrace and followed by lateral step propagation. Low aspect ratio disk-shaped islands are obtained with low step propagation rates and a small number of participating steps to slow down vertical growth. At the same time, fast surface diffusion on the substrate and a high concentration of Cu adatoms are necessary to speed up lateral growth.

From these results we conclude that three criteria are essential to achieve low aspect ratio islands resulting from enhanced lateral growth: (i) a substrate that leads to a small nucleation overpotential, (ii) fast adatom surface diffusion on substrate to promote lateral growth, and (iii) preferential anion adsorption to stabilize the basal plane.

ACKNOWLEDGMENTS

We thank Dr. R. C. Cammarata and Dr. J. D. Erlebacher for helpful discussions, Dr. David Necas (Masaryk University) for assistance in AFM image analysis, Dr. Xi Wang and Jun Wu for assistance in TEM sample preparation and characterization, and Dr. Ingrid Shao (IBM) for supplying the ruthenium wafers.

[1] E. Budevski, G. Staikov, and W. J. Lorenz, *Electrochemical Phase Formation and Growth: An Introduction to the Initial Stages of Metal Deposition* (VCH, Weinheim, 1996).
[2] E. Budevski, G. Staikov, and W. J. Lorenz, Electrochim. Acta **45**, 2559 (2000).
[3] E. Budevski, V. Bostanov, and G. Staikov, Annu. Rev. Mater. Sci. **10**, 85 (1980).
[4] A. Milchev, *Electrocrystallization: Fundamentals of Nucleation and Growth* (Kluwer, Boston, MA, 2002).
[5] D. Kashchiev, *Nucleation: Basic Theory with Applications* (Butterworth-Heinemann, Oxford, 2000).
[6] G. Oskam, P. M. Vereecken, and P. C. Searson, J. Electrochem. Soc. **146**, 1436 (1999).
[7] G. Oskam and P. C. Searson, Surf. Sci. **446**, 103 (2000).
[8] A. Radisic, F. M. Ross, and P. C. Searson, J. Phys. Chem. B **110**, 7862 (2006).
[9] A. Radisic *et al.*, Nano Lett. **6**, 238 (2006).
[10] A. Radisic *et al.*, Surf. Sci. **600**, 1817 (2006).
[11] A. Radisic, A. C. West, and P. C. Searson, J. Electrochem. Soc. **149**, C94 (2002).
[12] E. C. Walter *et al.*, J. Phys. Chem. B **106**, 11407 (2002).
[13] E. J. Menke *et al.*, Nature Mater. **5**, 914 (2006).
[14] R. M. Penner, J. Phys. Chem. B **105**, 8672 (2001).
[15] M. Giesen and S. Baier, J. Phys.: Condens. Matter **13**, 5009 (2001).
[16] Q. Wu and D. Barkey, J. Electrochem. Soc. **144**, L261 (1997).
[17] E. Budevski, G. Staikov, and V. Bostanov, J. Cryst. Growth **29**, 316 (1975).
[18] H. E. Buckley, *Crystal Growth* (Wiley, New York, 1951).
[19] J. W. Mullin, *Crystallization* (Butterworth-Heinemann, Oxford, 2001).
[20] W. K. Burton, N. Cabrera, and F. C. Frank, Philos. Trans. R. Soc. London, Ser. A **243**, 299 (1951).
[21] T. Sugimoto, Adv. Colloid Interface Sci. **28**, 65 (1987).
[22] C. A. Orme *et al.*, Nature (London) **411**, 775 (2001).
[23] P. D. Ward, Science **308**, 1566 (2005).
[24] C. Burda *et al.*, Chem. Rev. (Washington, D.C.) **105**, 1025 (2005).
[25] R. Narayanan and M. A. El-Sayed, Nano Lett. **4**, 1343 (2004).
[26] M. A. El-Sayed, Acc. Chem. Res. **37**, 326 (2004).

[27] V. F. Puntes, K. M. Krishnan, and A. P. Alivisatos, Science **291**, 2115 (2001).
[28] C. J. Murphy *et al.*, J. Phys. Chem. B **109**, 13857 (2005).
[29] C. J. Murphy *et al.*, Inorg. Chem. **45**, 7544 (2006).
[30] H. Yu *et al.*, J. Am. Chem. Soc. **125**, 16168 (2003).
[31] Z. A. Peng and X. G. Peng, J. Am. Chem. Soc. **123**, 1389 (2001).
[32] L. Guo, A. Radisic, and P. C. Searson, J. Electrochem. Soc. **153**, C840 (2006).
[33] D. R. Lide, *CRC Handbook of Chemistry and Physics: A Ready-Reference Book of Chemical and Physical Data* (CRC, Boca Raton, FL, 1992).
[34] S. Thurgate and K. Wandelt, *Solid-Liquid Interfaces Macroscopic Phenomena, Microscopic Understanding* (Springer, Berlin, 2003).
[35] P. Broekmann *et al.*, J. Electroanal. Chem. **467**, 307 (1999).
[36] M. Avrami, J. Chem. Phys. **7**, 1103 (1939).
[37] M. Avrami, J. Chem. Phys. **8**, 212 (1940).
[38] M. Avrami, J. Chem. Phys. **9**, 177 (1941).
[39] C. Donner, Z. Phys. Chem. **220**, 265 (2006).
[40] L. Ratke and P. W. Voorhees, *Growth and Coarsening: Ostwald Ripening in Material Processing*, Zeitschrift Fur Physikalische Chemie-International Journal of Research in Physical Chemistry & Chemical Physics (Springer, Berlin, 2002).
[41] M. Giesen *et al.*, Electrochim. Acta **45**, 527 (1999).
[42] D. M. Kolb, R. Ullmann, and J. C. Ziegler, Electrochim. Acta **43**, 2751 (1998).
[43] S. Morin *et al.*, Phys. Rev. Lett. **83**, 5066 (1999).
[44] A. Radisic *et al.*, J. Electrochem. Soc. **148**, C41 (2001).
[45] L. Guo and P. C. Searson, Langmuir **24**, 10557 (2008).
[46] R. Liu *et al.*, Chem. Mater. **13**, 508 (2001).
[47] G. Oskam *et al.*, J. Phys. D **31**, 1927 (1998).
[48] M. B. Vukmirovic, R. L. Sabatini, and R. R. Adzic, Surf. Sci. **572**, 269 (2004).
[49] A. Radisic *et al.*, J. Electrochem. Soc. **150**, C362 (2003).
[50] H. C. Koo *et al.*, J. Electrochem. Soc. **155**, D389 (2008).
[51] K. Krug, J. Stettner, and O. M. Magnussen, Phys. Rev. Lett. **96**, 246101 (2006).
[52] M. Giesen *et al.*, Surf. Sci. **595**, 127 (2005).
[53] O. M. Magnussen, Chem. Rev. (Washington, D.C.) **102**, 679 (2002).